batteries

MDPI

Article

Design of Cuboidal $FeNi_2S_4$-rGO-MWCNTs Composite for Lithium-Ion Battery Anode Showing Excellent Half and Full Cell Performances

Atin Pramanik [1,2,*], Shreyasi Chattopadhyay [1,3], Goutam De [1,4] and Sourindra Mahanty [1]

[1] CSIR-Central Glass & Ceramic Research Institute, 196 Raja S. C. Mullick Road, Kolkata 700032, India
[2] Department of Materials Science and Nano Engineering, Rice University, Houston, TX 77005, USA
[3] School of Chemistry, University of St Andrews, Purdie Building, North Haugh, St Andrews KY16 9ST, Fife, Scotland, UK
[4] S. N. Bose National Centre for Basic Sciences, Salt Lake, Kolkata 700106, India
* Correspondence: atinpramanik1990@gmail.com or ap112@rice.edu

Abstract: Ternary metal sulfides are projected as advanced lithium-ion battery (LIB) anodes due to their superior electronic conductivity and specific capacity compared to their respective oxide counterparts. Herein, a porous composite of cuboidal $FeNi_2S_4$ (FNS) with 2D reduced graphene oxide (rGO) and 1D multi-walled carbon nanotubes (MWCNTs) (composite name: FNS@GC) synthesised by an in-situ single-step hydrothermal process. The 1D/2D combined thin carbon coatings on the $FeNi_2S_4$ prevent aggregation during battery performance by increasing conductivity and resisting the volume changes at lithiation/de-lithiation processes. Consequently, the FNS@GC composite exhibits a commending electrochemical performance with a charge capacity of 797 mAh g^{-1} and a first cycle coulombic efficiency of ~67% with reversible capacity restoration property and excellent long-term cycling stability. Furthermore, FNS@GC//$LiFePO_4$ full cell reveals its practical applicability as a LIB anode with a reversible capacity of 77 mAh g^{-1} at 50 mA g^{-1} current density.

Keywords: ternary metal sulfide; $FeNi_2S_4$; hydrothermal synthesis; lithium-ion battery anode; electrochemical energy storage

Citation: Pramanik, A.; Chattopadhyay, S.; De, G.; Mahanty, S. Design of Cuboidal $FeNi_2S_4$-rGO-MWCNTs Composite for Lithium-Ion Battery Anode Showing Excellent Half and Full Cell Performances. *Batteries* **2022**, *8*, 261. https://doi.org/10.3390/batteries8120261

Academic Editors: Simon Wiemers-Meyer and Richard Schmuch

Received: 3 October 2022
Accepted: 24 November 2022
Published: 29 November 2022

1. Introduction

Developing an alternative green, safe and efficient energy storage technology has become critical to outpace the rapid degradation of fossil fuels and the continuous increase of environmental pollution. Lithium-ion battery (LIB) has gained significant attention among the leading energy storage technologies due to its high power density and long cycle life for portable device applications as well as for electric vehicles (EVs) [1–3]. In battery technology, the anode is one of the crucial components. Graphitic carbon, used as a conventional anode, suffers from a low theoretical capacity (372 mAh g^{-1}) and poor performance due to the inherently slow diffusion of Li^+ ions into the carbon matrix. Thus, graphitic anodes cannot satisfy the demand for EV applications requiring high-rate performance. Therefore, researchers have extensively searched for alternative high-performance LIB anodes [2,4].

Over the past few decades, binary and ternary transition metal oxides (TMOs) have been explored as LIB anodes [4,5]. However, they still suffer from volume expansion, commonly associated with the conversion mechanism during the redox processes. This led the researchers towards binary and ternary metal sulfides (TMSs). As the two-metal redox was involved in ternary metal sulfide, whereas one metal redox centre was involved in binary metal sulfide, that is why TMSs have better electrochemical performance. This is because the metal-sulfur (M-S) bond is weaker than the metal-oxygen (M-O) bond which allows faster diffusion of ionic species through the elongated layers, therefore, restricts

severe volume expansion [6,7]. Compared to their oxide counterparts, TMSs have shown a comparatively lower bandgap and, thus, a relatively higher electrical conductivity [8]. Moreover, the inherent stability of the structure, together with good mechanical integrity, may withstand the volume expansion during the charge-discharge processes. Several TMSs have been tested for electrochemical applications, primarily as a supercapacitor, e.g., $NiCo_2S_4$ [9], $ZnCo_2S_4$ [10], $MnCo_2S_4$ [11], $FeNi_2S_4$ [12], Cu_2ZnSnS_4 [13] etc. Application of TMS as LIB anode has also been undertaken, but the number of studies is relatively lesser. In most of the studies, $NiCo_2S_4$ [9,14–16], are the preferred choice though a few pieces of literature are also available on other ternary sulfides such as $CuCo_2S_4$ [17–19], $NiTi_2S_4$ [6]. Song et al. [20] prepared a composite of hexagonal $NiCo_2S_4$ nanosheets and reduced graphene oxide, which achieved a 607 mAh g^{-1} specific capacity at 2000 mA g^{-1} current density. In contrast, Wu et al. [21] synthesised hollow nanowires of $NiCo_2S_4$ on carbon cloth and reported a charge capacity of 1198 mAh g^{-1} at a 500 mA g^{-1} current rate. Hydrothermally synthesised porous core-shell $CuCo_2S_4$ nanospheres [19] reveal a 773.7 mAh g^{-1} charge capacity at 1000 mA g^{-1} current rate, whereas $CuCo_2S_4$/rGO nanocomposites deliver 433 mAh g^{-1} specific capacity at 100 mA g^{-1} current density [18]. Recently, Kim et al. prepared $NiTi_2S_4$ nanocomposite that shows 635 mAh g^{-1} of specific charge capacity at 1000 mA g^{-1} current rate for 50 cycles [6]. Until now, only a single report was available on $FeNi_2S_4$ as a LIB anode. Guo et al. prepared agglomerated particles of $FeNi_2S_4$ quantum dot @carbon composites and achieved an excellent specific capacity of ~750 mAh g^{-1} at 500 mA g^{-1} current density at LIB anode. However, the composite suffers from cycling stability and rate capability [22].

The above studies show the potential of ternary metal sulfides. Still, the fundamental challenges, e.g., volume change, crack generation, aggregation, pulverisation, and side reactions with electrolytes at the time of continuous discharge/charge cycling performances, are yet to be overcome before they can be applied as commercial LIB anodes. Two notable routes are presently being pursued to unravel the problems: (1) by constructing nanostructures with suitable morphological features for retaining structural integrity and (2) by synthesising in-situ composites with several types of conductive carbon additives to improve charge transfer processes.

Herein, we report a simple single-step hydrothermal technique to prepare a composite of cuboidal-shaped $FeNi_2S_4$ with rGO and MWCNTs (FNS@GC) where both the pursued routes are coupled together. The unique microstructure offers a larger surface area than pristine material for efficient conversion reaction and buffer space for volume change during continuous cycling. Furthermore, it is expected that the combination of 1D- and 2D-carbon layers on FNC would accelerate the ion transfer faster in the composite material [23]. As a result, the composite material delivers a capacity of 797 mAh g^{-1} at a current density of 100 mA g^{-1} with excellent rate capability even when subjected to high current rates. We have also constructed a full cell by coupling the FNS@GC anode with a commercial $LiFePO_4$ cathode. The full cell exhibits a specific capacity of 77 mAh g^{-1} at a current density of 50 mA g^{-1} with steady cycling performance.

2. Experimental

2.1. Chemicals

Nickel (II) chloride hexahydrate, $NiCl_2$. $6H_2O$ (98%. Alfa Aesar, Germany), ferric (III) chloride hexahydrate, $FeCl_3$. $6H_2O$ (97%, Alfa Aesar), thiourea (99%, Sigma-Aldrich, Germany), ethanol (Alfa Aesar, Germany), graphene oxide, multi-walled carbon nanotubes, MWCNTs (purity 95%, ash content < 1.5%), MTI, USA). Ultrapure water was used for all the experiments. The water was obtained from a three-stage Millipore Mill-Q (Merck, Germany).

2.2. Synthesis of Cuboidal Shaped Porous $FeNi_2S_4$@rGO/MWCNTs (FNS@GC)

The detailed synthesis procedure of graphene oxide has been described in our previous report [24]. At first, 0.25 mg of graphene oxide and 25 mg of MWCNTs were added to a

50 mL ethanol-water (1:1 volume ratio) solution and constantly stirred for 30 min to make it disperse throughout the solution. Then two mmol of nickel chloride hexahydrate and one mmol of ferric hexahydrate were added to that solution with continuous stirring. The stirring was continued for another 30 min to make the mixture homogeneous. Finally, nine mmol of thiourea was added to the above solution under stirring conditions. The resulting homogeneously dispersed solution was placed in a 70 mL Teflon-lined autoclave and kept in a 180 °C oven for 24 h. The autoclave was taken out manually after 24 h and cooled down to room temperature naturally. Next, the product was washed with deionised water and acetone several times and dried at 80 °C for 12 h in a vacuum oven.

The same procedure was followed to synthesise pristine FNS without using graphene oxide and a multi-walled carbon nanotube.

2.3. Material Characterisation

Powder X-ray diffraction was carried out using Philips X'Pert, the Netherlands X-ray diffractometer in 10°–80° 2θ range at 2° min^{-1} scan rate with Cu-Kα radiation at 40 kV and 40 mA. Renishaw in Via Reflex micro Raman spectrometer was used to record Raman spectroscopy with 514 nm argon-ion laser excitation. The morphological analysis was done by ZEISS Supra 35 (Germany) field emission scanning electron microscope (FESEM) and 300 kV Tecnai G2 30ST (FEI) transmission electron microscope (TEM). A Quantachrome (USA) Autosorb surface analyser was used to record Brunauer–Emmett–Teller (BET) surface area measurements using nitrogen gas adsorption at 77 K. The pore size distribution was calculated from the Barrett-Joyner-Halenda (BJH) desorption isotherm.

2.4. Electrochemical Characterisation

Two thousand thirty-two type coin cells vs Li/Li^+ were fabricated to measure the electrochemical properties of the sample. The standard slurry casting technique was followed to prepare the working electrode. The slurry was prepared using active material, Super-P carbon and polyvinylidene fluoride (PVDF) binder, in a weight ratio of 80:10:10 in n-methyl pyrrolidinone (NMP) solvent. The homogeneous slurry was coated on a copper foil (thickness 15 μm) and dried in a vacuum oven at 110 °C for 4 h. The coated copper foil was pressed at 4.0 tons per sq. inch for calendaring, and the electrodes were cut into a circular disk (dia. = 15 mm). The active mass loading was ~2 mg cm^{-2}, which is acceptable on the lab scale [25,26], though a higher mass loading could be better for the industrial scale LIB application [27]. The electrodes were placed in an argon-filled glove box (M'BRAUN, Germany, moisture and oxygen levels were kept at <0.5 ppm). The 2032 half cells were assembled using shiny lithium metal as the counter electrode as well as reference electrode, Celgard 2300 as the separator and 1.0 M $LiPF_6$ in EC: DMC (1:2 vol%) the electrolyte (Millipore Sigma-Aldrich, Germany, battery grade, ≥99.99% trace metals basis). Commercial $LiFePO_4$ (MTI corporation, USA and average particle size is 3.5 ± 1.0 μm) as the counter electrode (cathode) to assemble full cells. The active mass ratio of the anode to cathode was about 1:5. A galvanostat potentiostat (PGSTAT30, Autolab, The Netherlands) was used to record cyclic voltammetry (CV) at a scanning rate of 0.1 and 1.0 mV s^{-1}. Galvanostatic charge-discharge (GCD) experiments were recorded using an Arbin (BT2000, USA) automatic battery tester.

3. Results and Discussion

3.1. Physical Characterisation

Figure 1a shows the X-ray diffraction (XRD) pattern of the FNS@GC composite without any impure phase, and the diffraction peaks correspond to the characteristic reflections of $FeNi_2S_4$ (cubic phase, space group Fd3m) following the JCPDS file number 00-047-1740. The diffractogram exhibits very sharp peaks of the $FeNi_2S_4$, indicating excellent crystallinity of the synthesised compound. The most prominent diffraction peak was observed at a two-theta value of 31.51°, which originates from the reflections from the (311) planes of FNS@GC. The other main diffraction peaks at two theta values of 16.18°,

26.57°, 38.03°, 50.07°, and 54.8° correspond to the reflections from (111), (220), (400), (511), and (440) planes. A few other low-intensity peaks at two-theta values of 32.79°, 47.10°, 64.59°, 68.49°, and 77.33° correspond to the reflections from (222), (422), (533), (444), and (731) planes. However, the presence of a minute amount of impurity phases is suggested by the appearance of very low-intensity peaks at 18.21° and 35.42° (NiS, JCPDS file no. 00-012-0041) and at 27.93° and 36.75° (Fe_2S, JCPDS file no. 00-042-1340). Furthermore, we checked the X-ray diffraction (XRD) pattern of pristine FNS materials shown in Figure S1a.

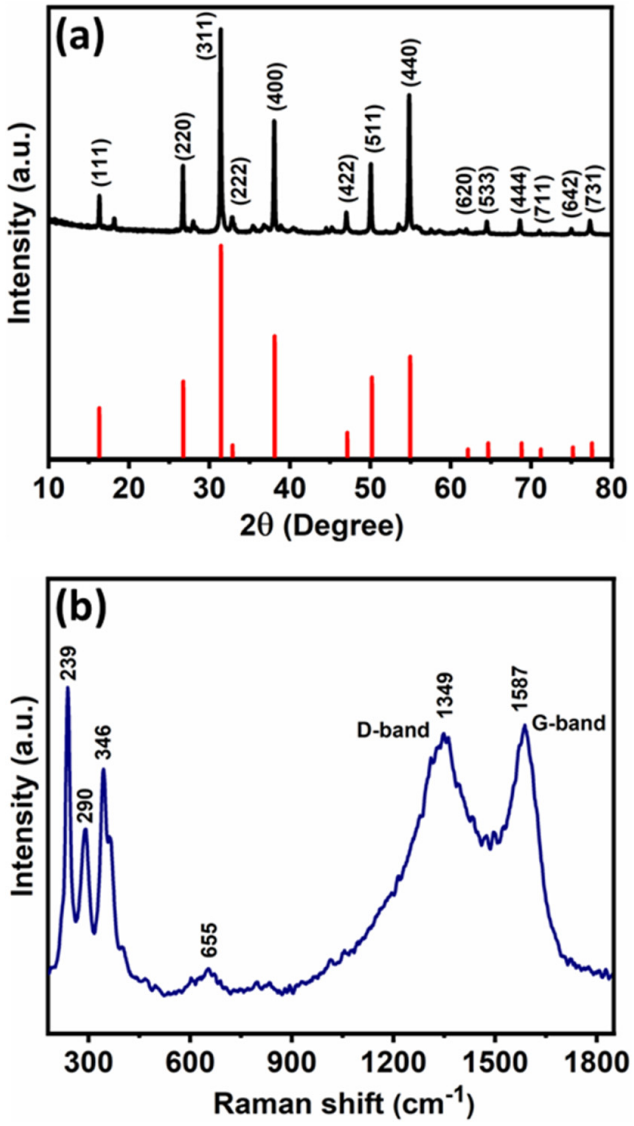

Figure 1. (**a**) Powder X-ray diffraction pattern, and (**b**) Raman spectra of FNS@GC composite.

Further, Raman spectroscopy was carried out for the FNS@GC composite (Figure 1b). The peak at 655 cm^{-1} could be assigned to Raman active A_{1g} modes. Two other prominent bands at 346 cm^{-1} and 239 cm^{-1} arise from the stretching modes of S atoms toward the tetrahedral site Fe atom and the bending of the S atoms initiating the A_{1g} and E_g modes, respectively [12,20,28]. The Raman bands at 290 cm^{-1} could be due to the asymmetric bending of S causing T_{2g} modes [28]. Two bands centred at 1349 and 1587 cm^{-1} were observed (Figure 1b) due to the well-known D-band and G-band originating from rGO [24]. It is noteworthy here that the synthesised graphene oxide (GO) shows two peaks at 1604 and 1360 cm^{-1}, which are assigned to the G-band and the D-band, respectively [26] (Figure S1b). The D and G-band intensity ratios denote the concentration of disorder or defect

and the average size of the p-conjugation [29]. The I_D/I_G ratio was 0.88 and 0.97, for GO and FNS@GC composite [30]. In the case of the FNS@GC composite, both the G-band and D-band are found to be shifted to a lower frequency region, i.e., toward the graphitic nature, therefore confirming the reduction of GO to rGO [24,30,31]. It is expected that the intensity of the D-band will gradually decrease when the GO is reduced. However, a higher I_D/I_G ratio suggests an intimate interaction between compound and carbon additives, follow-on in extra defects and destruction of sp^2 domains [31,32]. Such interaction would be favourable for faster charge transfer through defect-assisted propagation.

Electron microscopic analyses were carried out to evaluate the morphology of pristine FNS and FNS@GC. A FESEM image of the original 2D GO sheet is shown in Figure S2. The FESEM image of pristine FNS (Figure 2a) shows the formation of cuboidal to the near-spherical microstructure of size ranges <1–5 µm. The accumulation of such FNS particles leading to a composite structure is evident in the case of FNS@GC. The FESEM of FNS@GC (Figure 2b) shows FNS cuboidal and concurrent presence of 2D rGO sheets. However, it is hard to distinguish MWCNTs in FESEM because of intrinsic composite formation and the similar reflectivity of MWCNTs and rGO. For further understanding, TEM analysis of FNS@GC has been undertaken and shown in Figure 3. Figure 3a shows the rGO nanosheet and FNS particles of size ~1 µm. The magnified brightfield TEM image in Figure 3b exhibits the presence of 1D MWCNTs combined with rGO nanosheets. Furthermore, Figure 3c confirms the intrinsic composite structure showing the intimate presence of the three components, where the presence of 1D/2D C layers on FNS is seen. The FESEM energy dispersive X-ray spectrum of the synthesised FNS@GC powder (Figure S3) shows the presence of Fe, Ni, S, and C; the corresponding FESEM image is displayed in the inset. The TEM energy dispersive X-ray spectrum of the powder FNS@GC (Figure S4) further confirms the presence of the above elements.

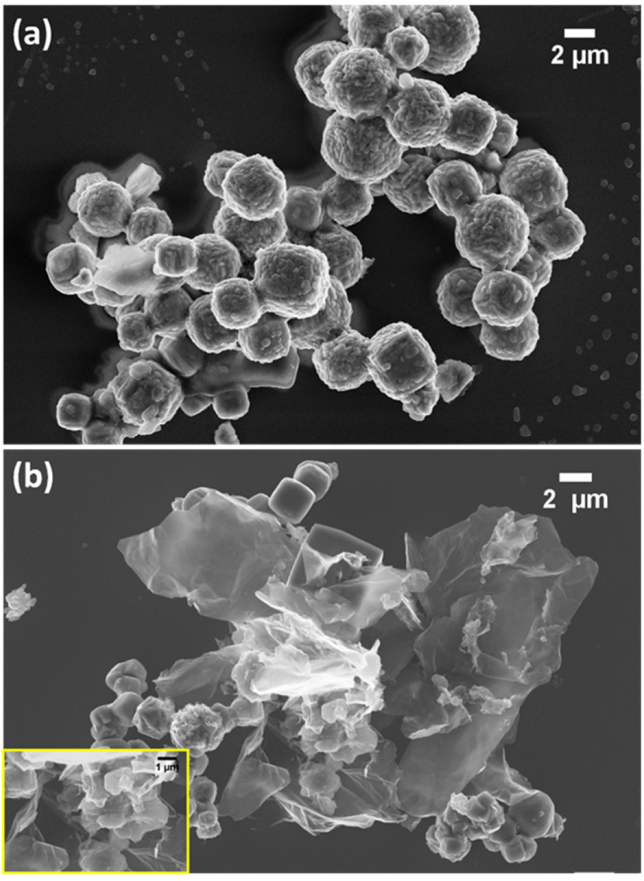

Figure 2. FESEM images for (**a**) pristine FNS and (**b**) FNS@GC composite powder (inset shows the magnified version of the FESEM image).

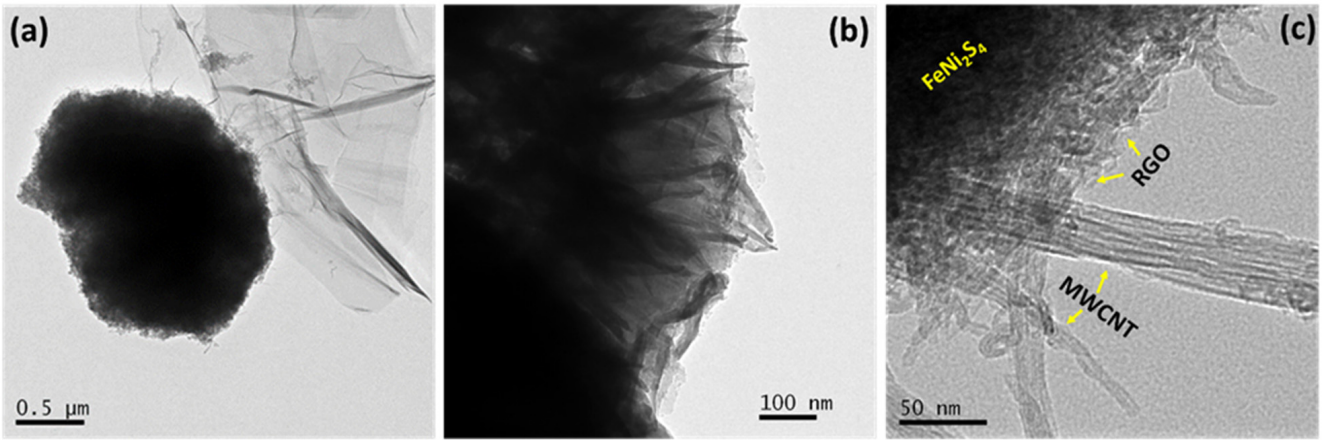

Figure 3. (**a**) TEM for FNS@GC composite, (**b**) magnified version of TEM image, and (**c**) further magnified image showing the integral presence of MWCNTs and rGO with $FeNi_2S_4$ particle.

Nitrogen adsorption-desorption isotherm and corresponding pore size distribution of both FNS and FNS@GC samples are presented in Figure 4. As shown in Figure 4a,b, the hysteresis loop of both FNS and FNS@GC reveals a typical type-IV isotherm characteristic of mesoporous materials. It is noted that the isotherms are not closed together at low pressures when P/P_0 returns to <0.4. This may happen due to residual adsorbed material in mesopore systems through irreversible uptake of molecules in pores of similar width as that of the adsorbate molecules, which are not outgassed [33]. The BET surface area of pristine FNS is only 18.2 m^2 g^{-1}, while for the FNS@GC composite, it increases to 31.4 m^2 g^{-1}. This increase in the surface area value for the composite is due to the contribution from rGO nanosheets and MWCNTs. The larger surface area allows effective electrolyte uptake and facilitates faster ion transfer. The corresponding pore size distribution plots were calculated from the adsorption branch of the isotherms and shown in the inset of Figure 4a,b. The pore volume of FNS@GC was more significant than that of pristine sample FNS, and the values were 0.023 and 0.009 cm^3 g^{-1}, respectively. Therefore, the porosity present in the material could act as buffering spaces against the volume changes of FNS during high-rate lithium/de-lithiation processes, which would lead to enhanced cycling stability of the anode material.

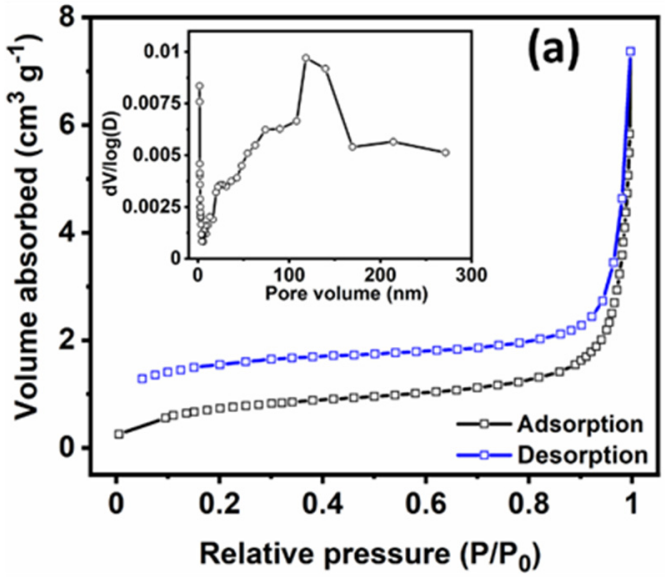

Figure 4. *Cont.*

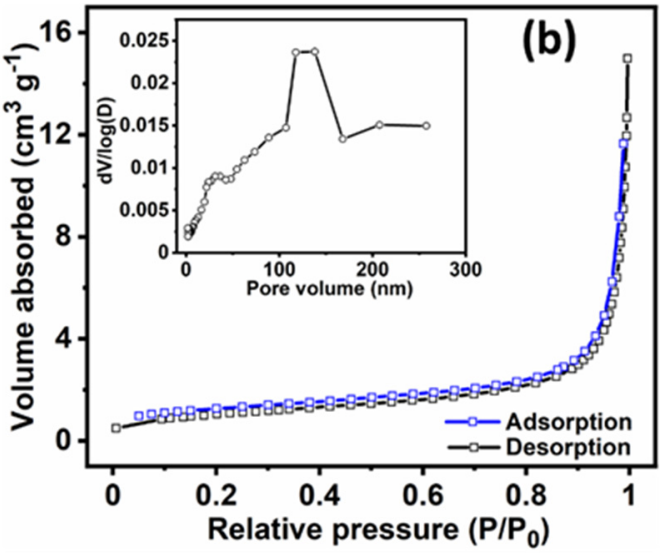

Figure 4. Nitrogen adsorption-desorption isotherms analysis and the inset shows corresponding pore size distribution, (**a**) pristine FNS and (**b**) FNS@GC.

3.2. Electrochemical Characterisation as Half Cell Lithium-Ion Battery (LIB) Anode

The lithiation/de-lithiation process of the FNS@GC has been carried out by assembling a 2032-type coin cell vs Li as the counter electrode. At first, the cyclic voltammetry (CV) test was performed for the half cell at a voltage window of 0.01–3.0 V at 0.1 mV s^{-1} scan rate (Figure 5a). Figure 6a shows the first four consecutive scans for the half cell. In the first discharge process, a weak peak is observed at 1.73 V that can be attributed to Li insertion in FNS@GC and the corresponding formation of Li_2FeS_2 [34]. The broad cathodic peak centred at 1.30 V can be attributed to the conversion of metal ions [20]. A hump is observed at 0.71 V, which confirms the decomposition of organic electrolyte and subsequent formation of solid electrolyte interphase layer (SEI) at the electrode-electrolyte interface, which is very common for LIB anode materials during the first cycle cathodic process [14,20,22]. At the first anodic scan, the peaks at 1.25, 2.0, 2.24, and 2.38 V can be attributed to the de-lithiation process and corresponding oxidation to FeS_x and NiS_x [20]. From the second cycle onwards, the CV of the cathodic scan is different from that observed in the first cycle, which is characteristic of conversion-based electrodes [35]. The appearance of one cathodic peak at 2.21 V (corresponding anodic peak at 2.35 V) can be attributed to the partial irreversible reduction of metal ions, which is missing from the third cycle onwards. That the prominent cathodic peaks are shifted from the second cycle onwards suggests possible irreversible structural changes of FNS@GC. The other three peaks at 1.82, 1.56, and 1.35 V correspond to the lithiation of the metal ions. The corresponding anodic peaks were observed at 1.25, 2.21, and 1.96 V due to the reversible oxidation process of the corresponding metal ions. From the third cycle onwards, no further change in the CV profile is observed, indicating good reversibility of the conversion-based lithiation/de-lithiation process in FNS@GC. Based on the above, the probable electrochemical conversion reaction of FNS@GC can be summarized as [22]:

First cycle discharge process:

$$FeNi_2S_4 + 8Li^+ + 8e^- \rightarrow Fe^0 + 2Ni^0 + 4Li_2S$$

The second cycle onwards:

$$FeS_x + 2xLi^+ + 2xe^- \leftrightarrow Fe^0 + xLi_2S$$

$$NiS_y + 2yLi^+ + 2ye^- \leftrightarrow Ni^0 + yLi_2S$$

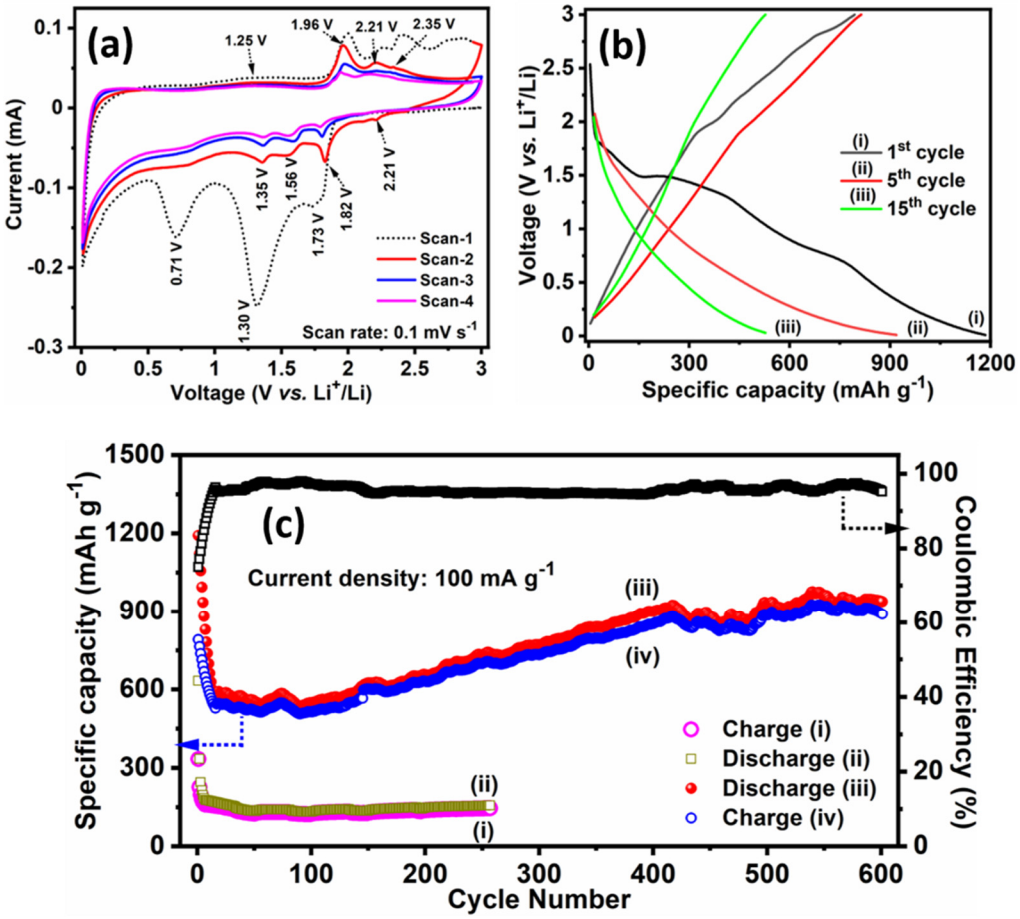

Figure 5. Half-cell LIB anode performance, (**a**) cyclic voltagram (CV) for first four cycles at 0.1 mV s^{-1} of FNS@GC electrode, (**b**) galvanostatic charge-discharge curves for 1st, 5th, and 15th cycles of FNS@GC and 1st cycle for FNS electrode at 100 mA g^{-1} current density at 0.01–3.0 V, and (**c**) cycling performance at 100 mA g^{-1} current rate for pristine FNS (i & ii) and FNS@GC electrodes (iii & iv).

The galvanostatic charge-discharge (GCD) for the FNS@GC sample was shown in Figure 5b in the same voltage window at a current density of 100 mA g^{-1} for the 1st, 5th, and 15th cycles. The GCD plots are consistent with the corresponding redox peaks observed in CV (Figure 5a). The first cycle-specific discharge and charge capacities were 1185 and 797 mAh g^{-1} with ~67% coulombic efficiency. Whereas the pristine FNS electrode shows first cycle discharge and charge capacity 629 and 361 mAh g^{-1}, respectively, with ~57% coulombic efficiency at 100 mA g^{-1} current density (Figure 5b). After a few cycles, the coulombic efficiency reaches ~98%, indicating the reversibility of the FNS@GC electrode during repeated lithiation/de-lithiation processes.

The cycling stability of a battery electrode is one of the essential criteria to judge its performance. Figure 5c shows the cyclicity test for pristine FNS and composite FNS@GC electrodes. The pristine FNS electrode shows capacity fading after a few cycles with a stable charge capacity of 149 mAh g^{-1} at the 100 mA g^{-1} current density (Figure 5c). Whereas the reversible capacity of the FNS@GC electrode initially decreases a little bit, but after a few cycles, when the electrode gets activated, the specific charge capacity increases to 906 mAh g^{-1} after 600 continuous cycles with ~96% coulombic efficiency at 100 mA g^{-1} current density (Figure 5c). These results are superior to the previously reported $FeNi_2S_4$ as LIB anode and other ternary metal sulfide anodes (Table 1) and ternary metal oxides (Table S1). The charge capacity increases to ~113% of the initial value, which implies excellent cycling performance. This phenomenon of increase in capacity is quite common for oxide/sulfide-based electrode materials associated with the formation and

decomposition of polymeric gel during the discharge and charge process [19,36–39]. These kinds of reversible growth of a polymer gel-like film originating from the degradation of electrolyte and extra lithium ion insertion/extraction into/from it has been reported in several works [19,36–40]. The increase in capacity with cycling could be attributed to FNS cuboidal dispersed in the gel matrix allowing better accommodation of volume changes and shortening of Li^+ diffusion length.

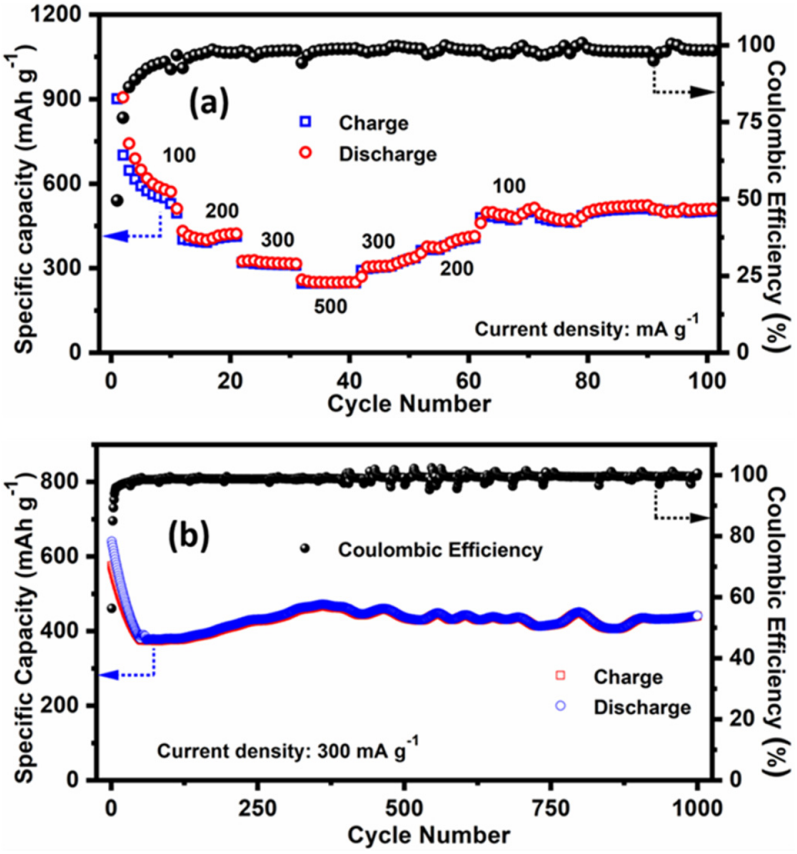

Figure 6. (**a**) Rate capabilities at different current densities (100 to 500 mA g^{-1}), and (**b**) long-life cycling performance at high current density (300 mA g^{-1}) with corresponding coulombic efficiency of FNS@GC electrode.

The capacity restoration property of FNS@GC has been investigated at different current densities by subjecting the cell to ten cycles at each current density, and the corresponding plot is shown in Figure 6a. At first, the assembled cell was cycled at 100 mA g^{-1} when a reversible capacity of ~578 mAh g^{-1} was observed. In the first few cycles, slight capacity decay was noticed due to the activation of the electrode. In the next step, when current densities are increased by two and three times, the reversible capacities ~425 and 324 mAh g^{-1} are observed. After that, when the current density increases by five times (500 mA g^{-1}), a specific capacity of 258 mAh g^{-1} is observed. To check the reversibility of the cell, the cell is then cycled again at 100 mA g^{-1}, and a reversible capacity of 519 mAh g^{-1} is observed, which is ~90% of the initial capacity. These results highlight a superior capacity restoration property of the FNS@GC electrode as a LIB anode.

To test the cycling performance at a high current rate, the FNS@GC has been cycled at a current density of 300 mA g^{-1} for 1000 continuous cycles (Figure 6b). The corresponding galvanostatic charge/discharge profiles of different cycle intervals are shown in Figure S5. The cell shows an initial minor decay incapacity. Still, after a few cycles, the capacity is recovered, and a reversible capacity of ~440 mAh g^{-1} was observed till 1000 cycles with the coulombic efficiency approaching ~100%.

Table 1. Comparison of Ternary metal sulfides as LIB anode application.

Materials	Morphology/Electrode Composition	Voltage Window (V)	Current Density (mA g^{-1})	Specific Capacity (mAh g^{-1})/Cycle Number	Ref.
$NiCo_2S_4$	hexagonal nanosheets@rGO	0.01–3.0	2000	607/800	[20]
$NiCo_2S_4$	hollow spheres	0.01–3.0	200	696/100	[41]
$NiCo_2S_4$	hollow nanowires@ carbon	0.005–3.0	500	1198/500	[21]
$NiCo_2S_4$	nanosheet array/carbon cloth	0.01–3.0	100	1137/100	[16]
$NiCo_2S_4$	nanocores in-situ encapsulated in graphene sheets	0.01–3.0	200	535/1000	[42]
$NiCo_2S_4$	multi-shelled hollow polyhedrons	0.0–3.0	100	745.5/100	[15]
$CuCo_2S_4$	agglomerated non-uniform nanoparticles/MWCNTs	0.01–3.0	500	1300/200	[17]
$CuCo_2S_4$	$CuCo_2S_4$/reduced graphene oxide nanocomposites	0.01–2.5	100	433/50	[18]
$CuCo_2S_4$	Sphere	0.01–3.0	1000	773.7/1000	[19]
$NiTi_2S_4$	nanoparticles	0.01–3.0	1000	635/50	[6]
$ZnCo_2S_4/NiCo_2S_4$	Flakes/@carbon cloth	0.01–3.0	1.5 mA cm^{-2}	2.4 mAh cm^{-2}/100	[25]
$FeNi_2S_4$	Agglomerated particle/$FeNi_2S_4$ quantum dot @C composites	0.005–3.0	500	~750/700	[22]
$(Fe_{0.5}Ni_{0.5})S_2$/rGO	0D/2D-sheet like nanocomposite	0.03–3.0	200	830/100	[43]
FNS@GC FNS@GC//$LiFePO_4$ (Full cell)	Cuboidal shaped FNS particle/with 1D/2D carbon composite	0.01–3.0 1.0–3.6	100 300 50	901/600 440/1000 77/60	This work

3.3. Electrochemical Performance of Full Cell LIB

Furthermore, inspired by the half-cell anode performance, we have assembled a full-cell battery (FNS@GC//$LiFePO_4$) using FNS@GC as anode and commercial $LiFePO_4$ as the cathode to verify the practical applicability of ternary metal sulfide as LIB anode. The detailed electrochemical characterization of commercial $LiFePO_4$ as half-cell LIB performance was shown in Figure S6a,b. At first, to check the active redox window, the CV test was done at 1.0–3.6 V voltage window at 1 mV s^{-1} scan rate, shown in Figure 7a. The CV for the first two cycles shows excellent reversibility where the voltammograms nearly overlap throughout the charge/discharge processes. Then, the GCD was plotted for the 1st, 5th and 15th cycles at 50 mA g^{-1} current density at 1.0–3.6 V voltage region (Figure 7b). As a result, the first cycle charge and discharge capacities were observed at 85 and 113.7 mAh g^{-1} with ~75% coulombic efficiency. The specific capacity was evaluated based on the active mass loading on the $LiFePO_4$ cathode electrode, as the capacity of the full cell is cathode-limited [26].

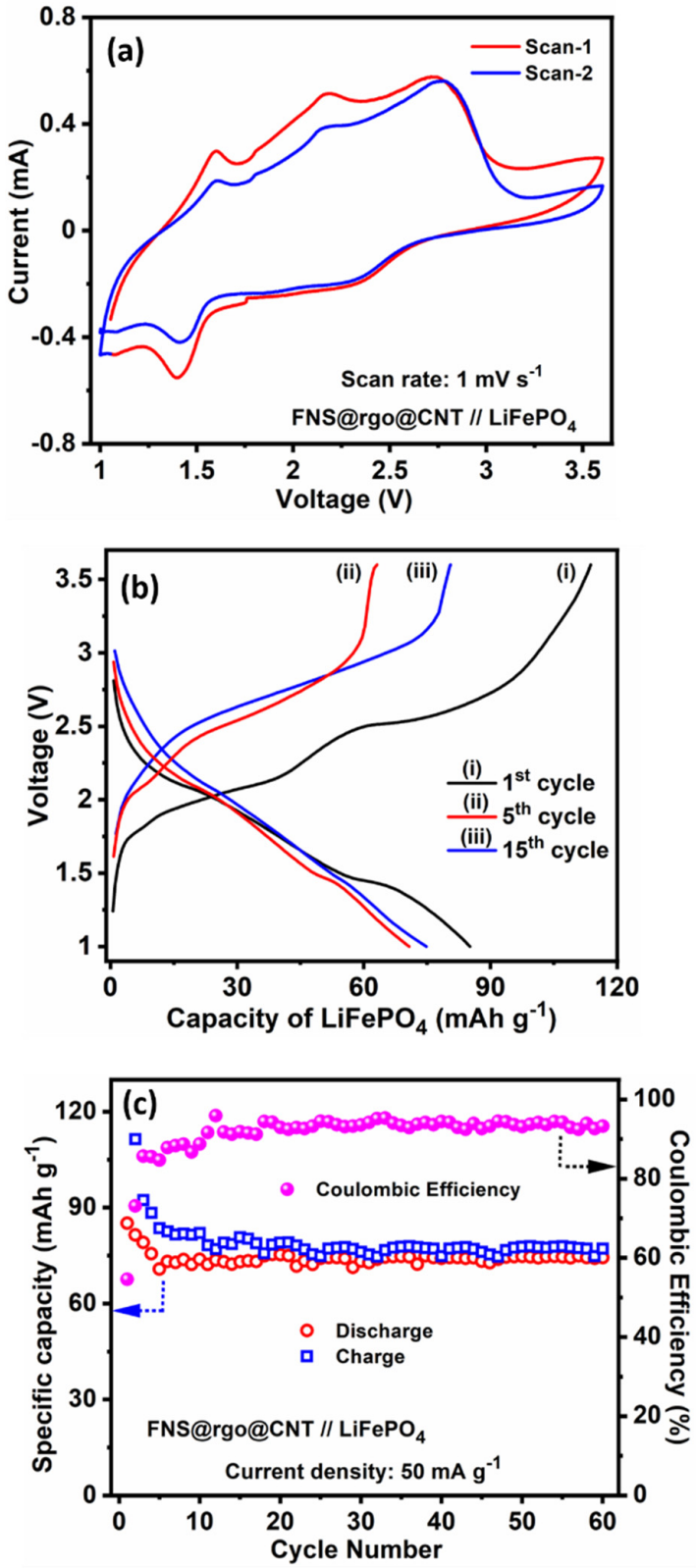

Figure 7. Full-cell LIB performance of FNS@GC electrode as anode and $LiFePO_4$ as cathode, (**a**) cyclic voltammogram (CV) for two cycles at 1 mV s^{-1} scan rate at 1.0–3.6 V voltage window, (**b**) galvanostatic charge-discharge curves for 1st, 5th, 15th cycles at 100 mA g^{-1} current density within 0.1–3.6 V, and (**c**) cycling stability performance at 50 mA g^{-1} current rate.

The cycling performance of the FNS@GC//$LiFePO_4$ full cell has been performed at 50 mA g^{-1} current density for 60 cycles (Figure 7c). The steady cycling plot shows excellent reversibility with observance of charge and discharge capacities of 77 and 74 mAh g^{-1}, respectively, together with a high coulombic efficiency of ~96%. There is no report on the full cell performance of $FeNi_2S_4$ as LIB anode; however, the present results are quite promising for the practical applicability of $FeNi_2S_4$ as LIB anode against $LiFePO_4$. However, no such report is available for metal sulfide as full cell LIB anode vs $LiFePO_4$. However, our full cell result is comparable with the other metal oxide-based materials vs $LiFePO_4$, where Si@MnO@C/rGO//LFP and Mn_3O_4@carbon//LFP show ~120 and ~92 mAh g^{-1} specific capacity at 5 C and 50 mA g^{-1} current rate, respectively [26,44].

4. Conclusions

In summary, a hierarchical composite of cuboidal-shaped porous $FeNi_2S_4$ ternary metal sulfide with MWCNTs and rGO has been successfully synthesised hydrothermally by a template-free method in a single step. The tightly wrapped rGO and MWCNTs thin layers over $FeNi_2S_4$ particles provide mechanical sustenance for the cuboidal structure, preventing particle detachment induced by repeated insertion/extraction of metal ions. Due to that, the space between the particles offers a passage for metal ions and electrolyte mobility. Furthermore, highly conductive carbon additives like rGO and MWCNTs facilitate charge transport during continuous high-rate charge/discharge processes. As a result, the FNS@GC shows high charge capacities of 906 mAh g^{-1} after 600 cycles at 100 mA g^{-1}. Furthermore, the composite shows a discharge capacity of 446 mAh g^{-1} at a high current density of 300 mA g^{-1} after 1000 cycles. In addition, a full cell comprising of the synthesised FNS@GC anode and commercial $LiFePO_4$ cathode reveals a stable cycling performance up to 60 cycles with 77 mAh g^{-1} of reversible capacity at 50 mA g^{-1} current density. The present results show promising potential for $FeNi_2S_4$ as a high-performance LIB anode and would help design other ternary metal sulphide anodes for energy storage applications.

Supplementary Materials: The following supporting information can be downloaded at: https://www.mdpi.com/article/10.3390/batteries8120261/s1. XRD pattern and Raman spectrum (Figure S1) of pristine FNS and GO, FESEM (Figure S2) of GO, FESEM-EDS of FNS@GC (Figure S3), TEM-EDS of FNS@GC (Figure S4), Galvanostatic charge-discharge curves for different cycle intervals of FNS@GC (Figure S5), $LiFePO_4$//Li half-cell electrochemistry plots (Figure S6) and comparison of Ternary metal oxides as LIB anode application (Table S1) [45–51].

Author Contributions: A.P.: Conceptualisation, Methodology, Writing—original draft. S.C.: Methodology, Writing. G.D.: Writing—review & editing. S.M.: Conceptualisation, Writing—review & editing. All authors have read and agreed to the published version of the manuscript.

Funding: A.P. thanks CSIR India for the senior research fellowship (Award Nos. 31/15(136)/2017-EMR-I). S.C. thanks UGC, India, for the research fellowship (Award No. F.2-44/2011(SA-I)).

Acknowledgments: A.P. thanks CSIR India and S.C. thanks UGC, India, for the research fellowship.

Conflicts of Interest: The authors declare no competing financial interests.

References

1. Tarascon, J.-M.; Armand, M. Issues and Challenges Facing Rechargeable Lithium Batteries. *Nature* **2001**, *414*, 359–367. [CrossRef]
2. Wu, F.; Maier, J.; Yu, Y. Guidelines and Trends for Next-Generation Rechargeable Lithium and Lithium-Ion Batteries. *Chem. Soc. Rev.* **2020**, *49*, 1569–1614. [CrossRef] [PubMed]
3. Lv, Z.; Wang, C.; Wan, C.; Wang, R.; Dai, X.; Wei, J.; Xia, H.; Li, W.; Zhang, W.; Cao, S.; et al. Strain-Driven Auto-Detachable Patterning of Flexible Electrodes. *Adv. Mater.* **2022**, *34*, 2202877. [CrossRef] [PubMed]
4. Grey, C.P.; Hall, D.S. Prospects for Lithium-Ion Batteries and beyond—a 2030 Vision. *Nat. Commun.* **2020**, *11*, 1–4. [CrossRef]
5. Nzereogu, P.U.; Omah, A.D.; Ezema, F.I.; Iwuoha, E.I.; Nwanya, A.C. Anode Materials for Lithium-Ion Batteries: A Review. *Appl. Surf. Sci. Adv.* **2022**, *9*, 100233. [CrossRef]
6. Kim, H.-H.; Kim, K.-H.; Lee, J.; Hong, S.-H. Electrochemical Properties and Reaction Mechanism of NiTi2S4 Ternary Metal Sulfide as an Anode for Lithium Ion Battery. *ACS Sustain. Chem. Eng.* **2021**, *9*, 9680–9688. [CrossRef]

7. Reddy, M.V.; Subba Rao, G.V.; Chowdari, B.V.R. Metal Oxides and Oxysalts as Anode Materials for Li Ion Batteries. *Chem. Rev.* **2013**, *113*, 5364–5457. [CrossRef] [PubMed]
8. Zhao, J.; Zhang, Y.; Wang, Y.; Li, H.; Peng, Y. The Application of Nanostructured Transition Metal Sulfides as Anodes for Lithium Ion Batteries. *J. Energy Chem.* **2018**, *27*, 1536–1554. [CrossRef]
9. Yi, T.F.; Pan, J.J.; Wei, T.T.; Li, Y.; Cao, G. NiCo2S4-Based Nanocomposites for Energy Storage in Supercapacitors and Batteries. *Nano Today* **2020**, *33*, 100894. [CrossRef]
10. Pramanik, A.; Maiti, S.; Dhawa, T.; Sreemany, M.; Mahanty, S. High Faradaic Charge Storage in ZnCo2S4 Film on Ni-Foam with a Hetero-Dimensional Microstructure for Hybrid Supercapacitor. *Mater. Today Energy* **2018**, *9*, 416–427. [CrossRef]
11. Pramanik, A.; Maiti, S.; Sreemany, M.; Mahanty, S. Carbon Doped MnCo2S4 Microcubes Grown on Ni Foam as High Energy Density Faradaic Electrode. *Electrochim. Acta* **2016**, *213*, 672–679. [CrossRef]
12. Pramanik, A.; Maiti, S.; Chattopadhyay, S.; De, G.; Mahanty, S. 'Cotton-Ball' Shaped Porous Iron-Nickel Sulfide: A High-Rate Cathode for Long-Life Aqueous Rechargeable Battery. *Mater. Res. Bull.* **2021**, *140*, 111307. [CrossRef]
13. Venugopal, B.; Shown, I.; Samireddi, S.; Syum, Z.; Krishnamoorthy, V.; Wu, H.L.; Chu, C.W.; Lee, C.H.; Chen, L.C.; Chen, K.H. Microstructural Intra-Granular Cracking in Cu2ZnSnS4@C Thin-Film Anode Enhanced the Electrochemical Performance in Lithium-Ion Battery Applications. *Mater. Adv.* **2021**, *2*, 5672–5685. [CrossRef]
14. Zuo, X.; Song, Y.; Zhen, M. Carbon-Coated NiCo2S4 Multi-Shelled Hollow Microspheres with Porous Structures for High Rate Lithium Ion Battery Applications. *Appl. Surf. Sci.* **2020**, *500*, 144000. [CrossRef]
15. Yuan, Y.F.; Ye, L.W.; Zhang, D.; Chen, F.; Zhu, M.; Wang, L.N.; Yin, S.M.; Cai, G.S.; Guo, S.Y. NiCo2S4 Multi-Shelled Hollow Polyhedrons as High-Performance Anode Materials for Lithium-Ion Batteries. *Electrochim. Acta* **2019**, *299*, 289–297. [CrossRef]
16. Zou, R.; Zhang, Z.; Yuen, M.F.; Sun, M.; Hu, J.; Lee, C.S.; Zhang, W. Three-Dimensional-Networked NiCo2S4 Nanosheet Array/Carbon Cloth Anodes for High-Performance Lithium-Ion Batteries. *NPG Asia Mater.* **2015**, *7*, 1–8. [CrossRef]
17. Muralidharan, N.; Nallathamby, K. CuCo2S4: Versatile Anode for High Capacity and High Rate for Lithium and Sodium Ion Battery Application. *J. Phys. Chem. Solids* **2021**, *151*, 109902. [CrossRef]
18. Gong, Y.; Zhao, J.; Wang, H.; Xu, J. CuCo2S4/Reduced Graphene Oxide Nanocomposites Synthesized by One-Step Solvothermal Method as Anode Materials for Sodium Ion Batteries. *Electrochim. Acta* **2018**, *292*, 895–902. [CrossRef]
19. Zheng, T.; Li, G.; Meng, X.; Li, S.; Ren, M. Porous Core–Shell CuCo2S4 Nanospheres as Anode Material for Enhanced Lithium-Ion Batteries. *Chem. A Eur. J.* **2019**, *25*, 885–891. [CrossRef]
20. Song, Y.; Chen, Z.; Li, Y.; Wang, Q.; Fang, F.; Zhou, Y.N.; Hu, L.; Sun, D. Pseudocapacitance-Tuned High-Rate and Long-Term Cyclability of NiCo2S4 Hexagonal Nanosheets Prepared by Vapor Transformation for Lithium Storage. *J. Mater. Chem. A* **2017**, *5*, 9022–9031. [CrossRef]
21. Wu, X.; Li, S.; Wang, B.; Liu, J.; Yu, M. Long-Term Cycling Stability of NiCo2S4 Hollow Nanowires Supported on Biomass-Derived Ultrathin N-Doped Carbon 3D Networks as an Anode for Lithium-Ion Batteries. *Chem. Commun.* **2021**, *57*, 1002–1005. [CrossRef] [PubMed]
22. Guo, P.; Song, H.; Liu, Y.; Wang, C. FeNi2S4 QDs @C Composites as a High Capacity and Long Life Anode Material for Lithium Ion Battery and Ex Situ Investigation of Electrochemical Mechanism. *Electrochim. Acta* **2017**, *258*, 1173–1181. [CrossRef]
23. Sun, Y.; Yang, Y.; Shi, X.L.; Suo, G.; Chen, H.; Noman, M.; Tao, X.; Chen, Z.G. Hierarchical SnS2/Carbon Nanotube@reduced Graphene Oxide Composite as an Anode for Ultra-Stable Sodium-Ion Batteries. *Chem. Eng. J. Adv.* **2020**, *4*, 100053. [CrossRef]
24. Pramanik, A.; Maiti, S.; Mahanty, S. Reduced Graphene Oxide Anchored Cu(OH)2 as a High Performance Electrochemical Supercapacitor. *Dalt. Trans.* **2015**, *44*, 14604–14612. [CrossRef] [PubMed]
25. Zhang, H.; Liu, J.; Lin, X.; Han, T.; Cheng, M.; Long, J.; Li, J. A Novel Binary Metal Sulfide Hybrid Li-Ion Battery Anode: Three-Dimensional ZnCo2S4/NiCo2S4 Derived from Metal-Organic Foams Enables an Improved Electron Transfer and Ion Diffusion Performance. *J. Alloys Compd.* **2020**, *817*, 153293. [CrossRef]
26. Pramanik, A.; Maiti, S.; Sreemany, M.; Mahanty, S. Rock-Salt-Templated Mn3O4 Nanoparticles Encapsulated in a Mesoporous 2D Carbon Matrix: A High Rate 2 V Anode for Lithium-Ion Batteries with Extraordinary Cycling Stability. *ChemistrySelect* **2017**, *2*, 7854–7864. [CrossRef]
27. Gogotsi, Y.; Simon, P. True Performance Metrics in Electrochemical Energy Storage. *Science* **2011**, *334*, 917–918. [CrossRef]
28. Jiang, J.; Lu, S.; Wang, W.K.; Huang, G.X.; Huang, B.C.; Zhang, F.; Zhang, Y.J.; Yu, H.Q. Ultrahigh Electrocatalytic Oxygen Evolution by Iron-Nickel Sulfide Nanosheets/Reduced Graphene Oxide Nanohybrids with an Optimized Autoxidation Process. *Nano Energy* **2018**, *43*, 300–309. [CrossRef]
29. Ye, Y.; Wang, P.; Dai, E.; Liu, J.; Tian, Z.; Liang, C.; Shao, G. A Novel Reduction Approach to Fabricate Quantum-Sized SnO 2-Conjugated Reduced Graphene Oxide Nanocomposites as Non-Enzymatic Glucose Sensors. *Phys. Chem. Chem. Phys.* **2014**, *16*, 8801–8807. [CrossRef]
30. Kudin, K.N.; Ozbas, B.; Schniepp, H.C.; Prud'homme, R.K.; Aksay, I.A.; Car, R. Raman Spectra of Graphite Oxide and Functionalized Graphene Sheets. *Nano Lett.* **2008**, *8*, 36–41. [CrossRef]
31. Yang, Y.; Ren, L.; Zhang, C.; Huang, S.; Liu, T. Facile Fabrication of Functionalized Graphene Sheets (FGS)/ZnO Nanocomposites with Photocatalytic Property. *ACS Appl. Mater. Interfaces* **2011**, *3*, 2779–2785. [CrossRef] [PubMed]
32. Pramanik, A.; Maiti, S.; Mahanty, S. Superior Lithium Storage Properties of Fe2(MoO4)3/MWCNT Composite with a Nanoparticle (0D)–Nanorod (1D) Hetero-Dimensional Morphology. *Chem. Eng. J.* **2017**, *307*, 239–248. [CrossRef]

33. Sing, K.S.W.; Everett, D.H.; Haul, R.A.W.; Moscou, L.; Pierotti, R.A.; Rouquerol, J.; Siemieniewska, T. Reporting Physisorption Data for Gas/Solid Systems with Special Reference to the Determination of Surface Area and Porosity. *Pure Appl. Chem.* **1985**, *57*, 603–619. [CrossRef]
34. Xu, C.; Zeng, Y.; Rui, X.; Xiao, N.; Zhu, J.; Zhang, W.; Chen, J.; Liu, W.; Tan, H.; Hoon Hng, H.; et al. Controlled Soft-Template Synthesis of Ultrathin C@FeS Nanosheets with High-Li-Storage Performance. *ACS Nano* **2012**, *6*, 4713–4721. [CrossRef] [PubMed]
35. Pramanik, A.; Maiti, S.; Mahanty, S. Metal Hydroxides as a Conversion Electrode for Lithium-Ion Batteries: A Case Study with a $Cu(OH)_2$ Nanoflower Array. *J. Mater. Chem. A* **2014**, *2*, 18515–18522. [CrossRef]
36. Pramanik, A.; Maiti, S.; Sreemany, M.; Mahanty, S. High Electrochemical Energy Storage in Self-Assembled Nest-like CoO Nanofibers with Long Cycle Life. *J. Nanoparticle Res.* **2016**, *18*, 93. [CrossRef]
37. Laruelle, S.; Grugeon, S.; Poizot, P.; Dollé, M.; Dupont, L.; Tarascon, J.-M. On the Origin of the Extra Electrochemical Capacity Displayed by MO/Li Cells at Low Potential. *J. Electrochem. Soc.* **2002**, *149*, A627. [CrossRef]
38. Zhou, G.; Wang, D.W.; Li, F.; Zhang, L.; Li, N.; Wu, Z.S.; Wen, L.; Lu, G.Q.; Cheng, H.M. Graphene-Wrapped Fe3O4 Anode Material with Improved Reversible Capacity and Cyclic Stability for Lithium Ion Batteries. *Chem. Mater.* **2010**, *22*, 5306–5313. [CrossRef]
39. Liu, C.; Zhang, T.; Cao, L.; Luo, K. High-Capacity Anode Material for Lithium-Ion Batteries with a Core-Shell NiFe2O4/Reduced Graphene Oxide Heterostructure. *ACS Omega* **2021**, *6*, 25269–25276. [CrossRef]
40. Luo, J.; Li, H.; Yu, G.; Xu, W.; Yin, H.; Hou, Z. Multifunctional Sandwich-Structured Double-Carbon-Layer Modified SnS Nanotubes with High Capacity and Stability for Li-Ion Batteries. *Mater. Adv.* **2022**, *3*, 3631. [CrossRef]
41. Jin, R.; Liu, D.; Liu, C.; Liu, G. Hierarchical NiCo2S4 Hollow Spheres as a High Performance Anode for Lithium Ion Batteries. *RSC Adv.* **2015**, *5*, 84711–84717. [CrossRef]
42. Chen, H.; Ma, X.; Shen, P.K. NiCo2S4 Nanocores In-Situ Encapsulated in Graphene Sheets as Anode Materials for Lithium-Ion Batteries. *Chem. Eng. J.* **2019**, *364*, 167–176. [CrossRef]
43. Liu, T.; Li, L.; Zhang, L.; Cheng, B.; You, W.; Yu, J. 0D/2D (Fe0.5Ni0.5)S2/RGO Nanocomposite with Enhanced Supercapacitor and Lithium Ion Battery Performance. *J. Power Sources* **2019**, *426*, 266–274. [CrossRef]
44. Liu, D.H.; Lü, H.Y.; Wu, X.L.; Wang, J.; Yan, X.; Zhang, J.P.; Geng, H.; Zhang, Y.; Yan, Q. A New Strategy for Developing Superior Electrode Materials for Advanced Batteries: Using a Positive Cycling Trend to Compensate the Negative One to Achieve Ultralong Cycling Stability. *Nanoscale Horizons* **2016**, *1*, 496–501. [CrossRef]
45. Hu, L.-H.; Wu, F.Y.; Lin, C.T.; Khlobystov, A.N.; Li, L.J. Graphene-Modified LiFePO4 Cathode for Lithium Ion Battery beyond Theoretical Capacity. *Nat. Commun.* **2013**, *4*, 1687. [CrossRef]
46. Yuan, L.X.; Wang, Z.H.; Zhang, W.X.; Hu, X.L.; Chen, J.T.; Huang, Y.H.; Goodenough, J.B. Development and Challenges of $LiFePO_4$ Cathode Material for Lithium-Ion Batteries. *Energy Environ. Sci.* **2011**, *4*, 269–284. [CrossRef]
47. Nag, S.; Pramanik, A.; Shyamal Roy, S.M. Enhancement of Li^+ Ion Kinetics in Boehmite Nanofiber Coated Polypropylene Separator in LiFePO4 Cells. *J. Solid State Chem.* **2022**, *312*, 123214. [CrossRef]
48. Kakarla, A.K.; Narsimulu, D.; Yu, J.S. Two-dimensional porous NiCo2O4 nanostructures for use as advanced high-performance anode material in lithium-ion batteries. *J. Alloys Compd.* **2021**, *886*, 161224. [CrossRef]
49. Li, T.; Li, X.; Wang, Z.; Guo, H.; Li, Y. A novel NiCo2O4 anode morphology for lithium-ion batteries. *J. Mater. Chem. A* **2015**, *3*, 11970. [CrossRef]
50. Kang, Y.; Shi, H.; Zhang, Y.-H.; Shi, F.-N. High-performance ZnCo2O4 microsheets as an anode for lithium-ion batteries. *Chem. Commun.* **2021**, *57*, 10723. [CrossRef]
51. Zhu, L.; Li, F.; Yao, T.; Liu, T.; Wang, J.; Li, Y.; Lu, H.; Qian, R.; Liu, Y.; Wang, H. Electrospun MnCo2O4 Nanotubes as High-Performance Anode Materials for Lithium-Ion Batteries. *Energy Fuels* **2020**, *34*, 11574–11580. [CrossRef]